Measuring three dimensional strain and structural defects in a single InGaAs nanowire using coherent x-ray multi-angle Bragg projection ptychography

Megan Hill, Irene Calvo-Almazan, Marc Allain, Martin Holt, Andrew Ulvestad, Julian Treu, Gregor Koblmueller, C. Huang, Xiaojing Huang, Hanfei Yan, et al.

Measuring three dimensional strain and structural defects in a single InGaAs nanowire using coherent x-ray multi-angle Bragg projection ptychography

M. O. Hill,[†] I. Calvo-Almazan,[‡] M. Allain,[¶] M. V. Holt,[§] A. Ulvestad,[‡] J. Treu,[∥] G. Koblmüller,[∥] C. Huang,[†] X. Huang,[⊥] H. Yan,[⊥] E. Nazaretski,[⊥] Y. S. Chu,[⊥] G. B. Stephenson,[‡] V. Chamard,[¶] L. J. Lauhon,[*,†] and S. O. Hruszkewycz[*,‡]

[1] †*Department of Materials Science and Engineering, Northwestern University, Evanston, Illinois 60208, USA*

‡*Materials Science Division, Argonne National Laboratory, Argonne, Illinois 60439, USA*

¶*Aix-Marseille Univ, CNRS, Centrale Marseille, Institut Fresnel, Marseille 13013, France*

§*Center for Nanoscale Materials, Argonne National Laboratory, Argonne, Illinois 60439, USA*

∥*Walter Schottky Institut and Physik Department, Technische Universität München, Garching 85748, Germany*

⊥*National Synchrotron Light Source II, Brookhaven National Laboratory, Upton, New York 11973, USA*

E-mail: lauhon@northwestern.edu; shrus@anl.gov

Keywords: Bragg ptychography; coherent X-ray diffraction imaging; nanowire; III-V; strain imaging; stacking faults

Abstract

III-As nanowires are candidates for near infrared light emitters and detectors that can be directly integrated onto silicon. However, nanoscale to microscale variations in structure, composition, and strain within a given nanowire, as well as variations between nanowires, pose challenges to correlating microstructure with device performance. In this work, we utilize coherent nano-focused x-rays to characterize stacking defects and strain in a single InGaAs nanowire supported on Si. By reconstructing diffraction patterns from the $2\bar{1}\bar{1}0$ Bragg peak, we show that the lattice orientation varies along the length of the wire, while the strain field along the cross-section is largely unaffected, leaving the band structure unperturbed. Diffraction patterns from the $01\bar{1}0$ Bragg peak are reproducibly reconstructed to create three-dimensional images of stacking defects and associated lattice strains, revealing sharp planar boundaries between different crystal phases of wurtzite (WZ) structure that contribute to charge carrier scattering. Phase retrieval is made possible by developing multi-angle Bragg projection ptychography (maBPP) to accommodate coherent nanodiffraction patterns measured at arbitrary overlapping positions at multiple angles about a Bragg peak, eliminating the need for scan registration at different angles. The penetrating nature of x-ray radiation, together with the relaxed constraints of maBPP, will enable *in operando* imaging of nanowire devices.

Nonplanar semiconductor heterostructures provide opportunities for novel and efficient functionality over a broad range of applications. For example, ternary III-As nanowire heterostructures are promising near-IR emitter/detectors for applications including on-chip photonic information transfer due to their bandgap tunability and high electron mobility.[1–4] Additionally the nanowire geometry enables direct integration of III-V's onto silicon, as the small interface area mitigates the formation of dislocations and anti-phase domain boundaries.[5–7] However, III-As nanowires commonly exhibit nanoscale structural inhomogeneties such as stacking faults, polytype insertions, and nanofaceting.[8,9] In addition, composition fluctuations in ternary alloys and the resulting lattice strain can modify the electronic bandgap.[8,10,11] When nanoscale defects occur together with composition and strain variations on multiple lengthscales, it can be challenging to establish the physical origins of properties and device behaviors that are probed over microscale volumes. Therefore, the necessary optimization of nanowire materials for specific electronic and optoelectronic devices will require improved approaches to map local inhomogeneities in crystal structure and composition throughout a nanowire, preferably using approaches that enable *in operando* analysis.

Although the present work includes analysis of previously unreported perturbations in nanowire structure encompassing nanometer to micron lengthscales, we are especially motivated to probe structural features that strongly influence optical emission and electronic transport properties. In particular, there is a strong correlation between the density of stacking defects and mobility in III-As nanowires.[12,13] Comparing high resolution transmission electron microscopy (TEM) images of free standing nanowires with position dependent field effect mobility measurements on InAs nanowire devices, Schroer et al[12] showed that low densities of stacking faults localize electrons, leading to transport characteristics consistent with quantum dot formation even in devices with low resistance Ohmic contacts. Irber et al[13] later showed that diffusive quantum transport in quasi 1-D sub-bands can be observed in modulation doped GaAs nanowires even in the presence of stacking faults, but

as the stacking fault density increases, quantum features are washed out due to increased scattering. It is also well established that crystal phase switching between wurtzite (WZ) and zinc blende (ZB) polytypes, which exhibit a type II band alignment,[14] leads to the formation of quantum dots that act as single photon emitters.[15] Further, Jahn et al[14] observed that GaAs nanowires with the same average WZ/ZB content may luminesce above or below the ZB bandgap, dependent on the thickness of the ZB insertions. The interpretations advanced in the works cited above require *a priori* knowledge of the spatial variation in the density of stacking defects. Methods such as transmission electron microscopy have contributed greatly to our understanding of structure/property relationships in nanowires, and the development of complimentary approaches compatible with more complex sample environments (*e.g.* nanowire devices fabricated on standard Si wafers) is needed to deepen our understanding.

A promising avenue lies in coherent x-ray diffraction imaging (CDI), which offers the advantage of probing strain and other structural features in nanowires over a larger field of view on thicker substrates and embedded in operating devices. To date, 2D CDI methods have been used to view longitudinal projections[16] or cross sectional cuts[17–19] of lattice strain in III-V nanowires. However, scaling the approach to three dimensions and towards multi-scale imaging is not straightforward because high resolution in 3D is needed of a high-aspect-ratio sample. Existing 3D CDI techniques are not well suited for measuring extended structures such as nanowires that are larger than the x-ray beam footprint. Further, abruptly varying features, such as crystal phase switching at few-nanometers length scales in nanowires, cannot be reliably imaged using traditional CDI methods.[20,21]

Here we overcome the limitations of conventional 3D CDI by adapting Bragg ptychography, a variant of CDI based on scanning focused coherent x-ray beam measurements, to robustly reconstruct 3D images of strain and stacking defects in single InGaAs nanowires. The analysis focuses on InGaAs nanowires grown by catalyst-free molecular beam eptiaxy (MBE) which have been shown to have wide compositional tunability and can be used as

a foundation for epitaxial core-shell heterostructures[22,23] for near-IR optoelectronics. We demonstrate reconstruction of single stacking defects and lattice strain in InGaAs nanowires on Si substrates with a spatial resolution better than 3 nm. To do so, we introduce an implementation of Bragg ptychography (named multi-angle Bragg Projection Ptychography, maBPP) in combination with coarse-scanning Bragg nanodiffraction analysis to provide a holistic view of the hierarchical structure of a single InGaAs nanowire spanning from nanometers to several microns. The methodological framework we present, and the proof of principle we demonstrate, can enable new insights into the impact of stacking faults and crystal phase switching on the characteristics of individual substrate-supported nanowire devices *in operando*.

Prior to describing the data and analysis, we briefly introduce 3D Bragg ptychography and the motivation for the specific advance in methodology that was required to resolve single stacking faults in a nanowire with a high density of these defects. We utilize 3D Bragg ptychography as it satisfies many attributes necessary for characterizing complex III-V nanowires: nanoscale resolution, sensitivity to different structural features, and the potential for mapping extended crystals. With Bragg ptychography, nanoscale variations in crystal structure can be imaged by numerically inverting coherent diffraction intensity patterns measured in the vicinity of a Bragg peak.[24,25] The approach utilizes a localized scanning x-ray probe (typically focused with an x-ray optic) and entails measuring oversampled Bragg coherent diffraction patterns at different overlapping scan positions at one[24] or more[25] angles near the Bragg diffraction condition of an extended crystal. Gradient-based iterative inversion algorithms have been developed[26–28] to retrieve the phases (which cannot be measured experimentally) of the intensity patterns in such a data set and to provide a real-space image of the complex-valued structure factor of the measured Bragg peak. Variation in the phase of these structure factor images can then be interpreted in terms of various phenomena, including lattice displacement from elastic strain fields,[29] defects in atomic stacking order,[30,31] individual dislocations,[32] and ferroelectric polarization.[33] Typically, these phenomena can be

observed with a spatial resolution of 5-50 nm, depending on the signal-to-noise ratio (SNR) of the measurement and other factors such as scattering geometry, degree of probe overlap, and choice of reconstruction algorithm.[28]

Traditional 3D Bragg ptychography utilizes data sets with fine angular steps about the Bragg peak (known as rocking curves),[25,34] requiring that high SNR diffraction data be collected for all angles at each probe position. 3D reconstruction algorithms require that scan positions be commensurate at every diffraction angle to within a few percent of the beam diameter, a requirement that is highly challenging with state-of-the-art hard x-ray focusing optics that produce focii of <100 nm and operate in fly-scan mode.[35,36] Alternatively, methods such as Bragg projection ptychography (BPP and 3DBPP) have been developed that only require a single angle measurement. Scanning Bragg nanodiffraction data at a single-angle can then be inverted into 2D[37] and 3D[24] images of lattice structure within a material. However, single-angle 3D BPP requires high diffraction angles ($>\sim 60^\circ$) that can be difficult to reach experimentally and at which Bragg peaks scatter more weakly.

We address these challenges by utilizing a generalized 3D multi-angle Bragg projection ptychography approach, which is described in more detail in the Algorithm Description section. maBPP relaxes experimental constraints such that a set of coherent diffraction intensity patterns measured at arbitrary angles and positions can be incorporated into a single 3D reconstruction, without requiring any position registration. Specifically, we implement maBPP by adapting the Ptychographic Iterative Engine (PIE),[26] a phase retrieval algorithm shown to be well suited for ptychographic imaging.

$In_{0.86}Ga_{0.14}As$ nanowires with diameters of 100-200 nm were grown by catalyst-free molecular beam epitaxy under conditions similar to those in Reference 38. Nanowires of this diameter range, and even larger diameters, are of interest for IR optoelectronics because optical modes are insufficiently confined at smaller diameters.[39] HRTEM investigation of similar samples revealed a primarily WZ crystal phase with a high density of stacking faults, typically spaced by <10 nm. No extended regions (>1 nm) of ZB were observed at these

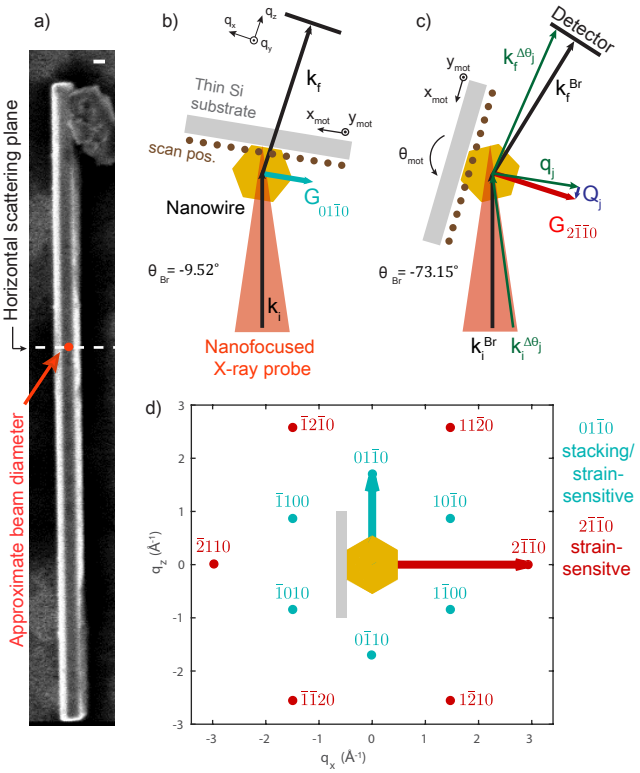

Figure 1: Experimental geometry at HXN beamline (a) SEM image of the investigated InGaAs nanowire. Scale bar is 100 nm. The focused x-ray probe (red circle) is approximately 50 nm in diameter. Scattering geometries used for the $01\bar{1}0$ (b) and $2\bar{1}\bar{1}0$ (c) conditions. θ_{Br} is the angle of the integrated intensity maximum of the rocking curve. k_i^{Br} and k_f^{Br} are the initial and final scattering vectors at θ_{Br}, defined by the momentum transfer vector G. $k_i^{\Delta\theta_j}$ and $k_f^{\Delta\theta_j}$ are the initial and final scattering vectors for the jth angle away from θ_{Br}, defined by the momentum transfer q_j, Q_{θ_j} away from G. (d) The reciprocal space lattice in the radial plane of the nanowire (cyan and red points) and a schematic of the facets of the InGaAs nanowire studied (yellow hexagon). The family of $2\bar{1}\bar{1}0$ peaks of the WZ lattice correspond to the $20\bar{2}$ family of peaks in the ZB structure, and they are sensitive to lattice strain fields within the nanowire. The $01\bar{1}0$ peaks have no analog in the cubic ZB structure. These peaks are sensitive to stacking faults in the WZ phase as well as a component of lattice strain. Bragg ptychography nanodiffraction area raster scans were performed on the same nanowire at the $2\bar{1}\bar{1}0$ and $01\bar{1}0$ Bragg peaks and reconstructed into complementary 3D images.

growth conditions.[38] To prepare a sample for structural imaging with maBPP, the nanowires were drop-casted onto a 10-μm-thick silicon substrate that transmits hard x-rays prepared for this application via selective etching and lithography by Norcada Inc., and the location of nanowires relative to chromium fiducial markers on the substrate was determined with scanning electron microscopy (SEM), prior to x-ray investigations. The SEM characterization revealed that each nanowire was fixed to the substrate with an a-plane $(2\bar{1}\bar{1}0)$ facet parallel to the Si surface. (We adopt hexagonal four-index notation in this work consistent with the hexagonal WZ crystal structure.) Figure 1(a) shows a SEM image of the 200-nm-diameter nanowire investigated.

Bragg ptychography coherent nanodiffraction measurements were performed at the Hard X-ray Nanoprobe (HXN) beamline of the National Synchrotron Light Source II (NSLS-II).[40–42] A coherently-illuminated x-ray zoneplate with an outermost zone width of 40 nm was used to focus 10.4 keV monochromatic x-rays at the sample, forming a minimum spot size of 49 nm with an 80 mm focal length. The wavefront of the probe was characterized with standard direct-beam ptychography of a known reference sample[27] prior to the nanowire measurements. Scanning probe fluorescence measurements were used to locate an individual nanowire with the long axis aligned vertically. The vertical nanowire orientation enabled two different Bragg peaks ($01\bar{1}0$ and $2\bar{1}\bar{1}0$) to be accessed in the horizontal scattering plane, each sensitive to a different structural component of the nanowire. Figure 1(b-d) shows depictions of the scattering geometries used to reach the Bragg peaks measured here, as well as their reciprocal space orientation. At both Bragg conditions, 2D nanodiffraction maps were measured at a series of angles about the Bragg peak while simultaneously measuring Ga K-edge fluorescence.

Positional scans were done in a fly-scan mode, moving the sample with motors oriented parallel to the Si membrane surface (x_{mot}, y_{mot} in Figure 1(c)), and the angle was adjusted in 0.02° steps about the Bragg condition with a rotational stage (θ_{mot}) that rotated the nanowire along its long axes. Fly scans, now being increasingly utilized for ptychography

measurements,[35] were implemented with an average dwell time per scan point of 0.2 seconds in order to minimize scan time overhead and eliminate motor settling time. A Merlin pixel array detector was used with 512×512 square pixels with 55μm edges and a sample-to-detector distance of 500 mm and 330 mm for the $2\bar{1}\bar{1}0$ and $01\bar{1}0$ Bragg peak measurements respectively. These peaks were found at θ motor positions of $\theta_{Br}^{2\bar{1}\bar{1}0} = -9.52°$ and $\theta_{Br}^{01\bar{1}0} = -73.15°$, with the detector positioned 33.7° and 19.04° off the direct beam respectively, as shown in Figure 1. At each angle, about both Bragg peaks, overview nanodiffraction raster maps measured with coarse step sizes ($\sim$ 100 nm) were performed of the entire wire, which was used to correct for error from uncertainty in the center of rotation of the θ motor. Then fine-stepped raster scans (step size $\sim$ 25 nm) were used for Bragg ptychography data in specific regions of the wire. We note that we did not attempt to register probe scan positions as a function of angle, as this would be impractically difficult for a 50 nm beam. This emphasizes the need for the new maBPP approach, which allows for incommensurate positions to be incorporated into the phase retrieval.

The two Bragg peak measurements in this study were chosen to image different types of lattice structure in the InGaAs nanowires via the sensitivity of the Bragg structure factor. As illustrated in Figure 1(d), the family of $01\bar{1}0$ Bragg peaks originate only from the hexagonal WZ phase (this peak is forbidden in the cubic ZB structure). As has been derived previously,[20,43] the structure factor of a WZ $01\bar{1}0$-type peak changes by $\pm 2\pi/3$ across a $\langle 0001 \rangle$ c-axis stacking fault. In addition to the spatial variations in structure factor from WZ stacking faults, any overall distortions of the crystal due to elastic strain, dislocations, etc. will also be encoded in the structure factor, and correspondingly in the phase of $01\bar{1}0$ Bragg ptychography reconstruction. The second Bragg peak belongs to the $(2\bar{1}\bar{1}0)$ family of WZ Bragg peaks which is not sensitive to WZ stacking faults, and is indistinguishable from the cubic ZB $(20\bar{2})$ type peaks. As a result, images derived from a $2\bar{1}\bar{1}0$ Bragg peak will reveal more subtle structural perturbations such as those due to elastic strain fields. In the remainder of the paper, we examine the qualitative differences between Bragg scattering

patterns measured at the $2\bar{1}\bar{1}0$ and $01\bar{1}0$ Bragg peaks, show an analysis of $2\bar{1}\bar{1}0$ diffraction that reveals micron-scale structure in the NW, and conclude by discussing 3D images of nanoscale strain fields and stacking order obtained from maBPP reconstructions of both Bragg conditions.

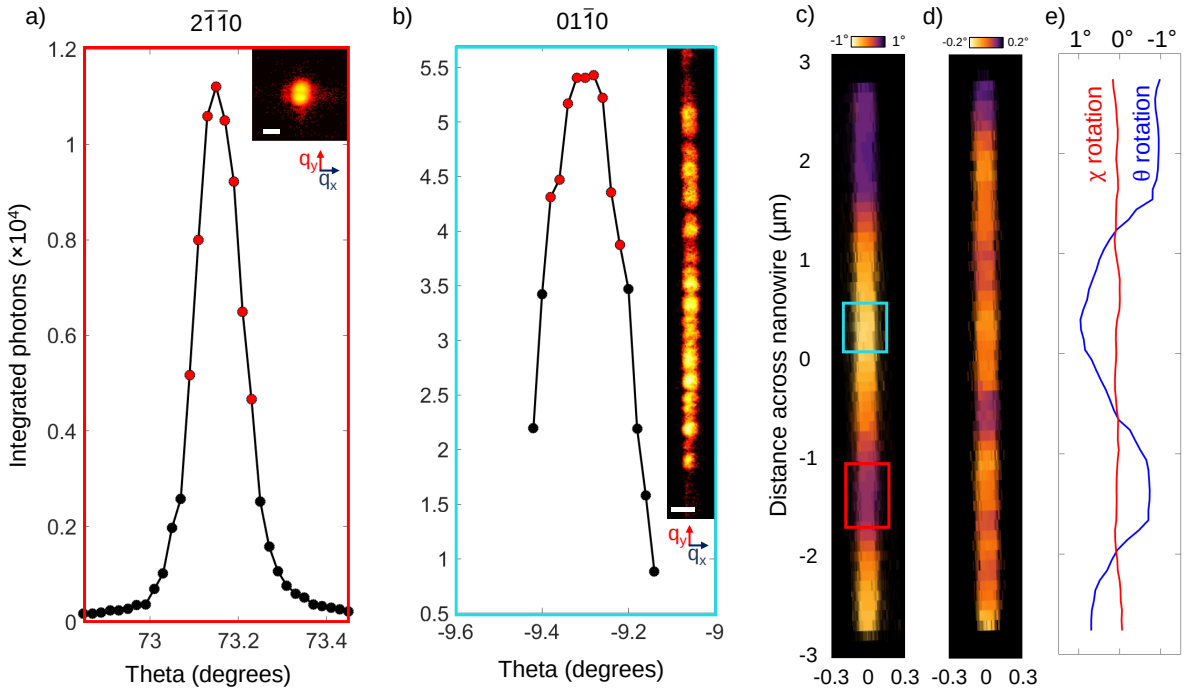

Figure 2: Sample rocking curves measured for the $2\bar{1}\bar{1}0$ (a) and $01\bar{1}0$ (b) peaks were taken taken from the center of red and cyan boxes in (c) respectively. Data was collected at each plotted point, but 3D maBPP reconstructions were performed in these regions using only the angles marked in red. Example 2D diffraction patterns (logarithmic intensity) at the Bragg maximum are shown in an inset. The diffraction pattern insets span different distances, with scale bars of 3 nm^{-1} (a) and 50 nm^{-1} (b). 2D diffraction peak mapping obtained from the $2\bar{1}\bar{1}0$ intensity patterns reveals a relative twist (c) about the long axis (about θ) and (d) a bending in the plane of the Si substrate (about χ) as a function of position across the nanowire. (e) 1D line cuts of twisting (blue) and bending (red) through the center of the nanowire. Variations in angle for (c),(d), and (e) are relative to their Bragg maximum near 73.15 degrees.

The characteristics of typical scattering patterns measured at both Bragg conditions highlight their sensitivity to different local structure in the nanowire. Figure 2(a,b) shows rocking curves of the $2\bar{1}\bar{1}0$ and $01\bar{1}0$ Bragg peaks measured near the middle of the outlined regions in Figure 2(c). (The rocking curves were obtained by first registering the series of 2D overview

nanodiffraction maps to one another using Ga fluorescence maps. The integrated-intensity rocking curves shown were then extracted from a fixed pixel position of the aligned nanowire fluorescence maps.) The coherent nanodiffraction patterns measured at the maxima of these rocking curves are inset in Figure 2. The diffraction pattern insets span different distances in qx, qy: (a) 15 nm^{-1}, 15 nm^{-1} and (b) 100 nm^{-1}, 1000 nm^{-1}. The $2\bar{1}\bar{1}0$ Bragg peak is predominantly composed of a central annulus-shaped speckle,[44] and can be used to map the orientation and spacing of the $(2\bar{1}\bar{1}0_{WZ})/(20\bar{2}_{ZB})$ lattice planes. By contrast, the diffraction pattern at the $01\bar{1}0$ Bragg peak is made up of many annular speckles scattering over a broad range of q_y originating from the closely spaced stacking fault boundaries illuminated by the beam that act as an interference grating.[43] Any variation in the position or intensity of individual annular speckles within the $01\bar{1}0$ peak encodes differences in the local arrangement and nature of stacking boundaries within the illuminated volume.

By extracting the angle and position of the $2\bar{1}\bar{1}0$ Bragg peak maximum from the coarse nanodiffraction maps (an analysis approach similar to previous work[45–47]), we find that the lattice orientation varies continuously as a function of position. Figure 2(c) shows the twisting of the nanowire about the θ axis (rotation about y_{mot} as defined in Figure 1(c)), while Figure 2(d) shows the rotation about the incident beam direction (denoted as χ rotation), which is extracted by mapping the $2\bar{1}\bar{1}0$ peak center of mass along q_y. From these maps, we found that the Bragg peak angle varied by $\pm \sim 1.0°$ from the mean in θ, indicating that the nanowire lattice is twisted along its growth axis. Variations of up to $\pm \sim 0.2°$ from the mean in χ also indicate a bending of the nanowire. We note that all nanowires examined showed bending and twisting of a similar magnitude that could arise either during growth or during transfer to the Si membrane substrate. Regardless, the above analysis provides a micron-scale view of the lattice structure that would be useful for monitoring, for example, strain within functioning nanowire devices, and from which one can "zoom in" to specific regions of interest with ptychography.

Further analysis based on the maBPP approach enables reconstruction of a higher-

resolution 3D image of strain, and furthermore, provides a means to invert the more complicated speckle patterns measured at the $01\bar{1}0$ Bragg peak into 3D real space images. The reconstructions were performed for the red and cyan regions marked in Figure 2(c) for the $2\bar{1}\bar{1}0$ and $01\bar{1}0$ Bragg peaks respectively. Different regions of the nanowire were imaged in order to avoid possible beam induced damage,[48] though later measurements reveal the nanowire was structurally robust under continuous focused x-ray probe exposure.

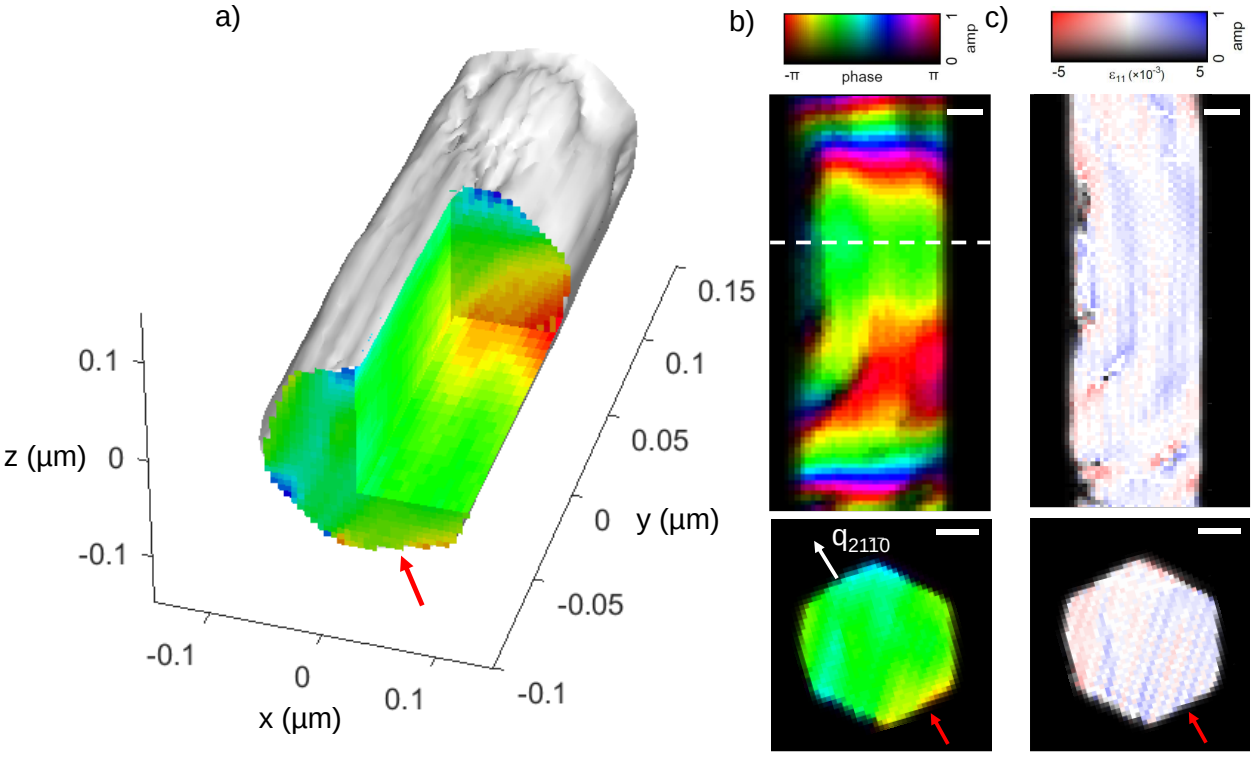

Figure 3: maBPP reconstruction of the $2\bar{1}\bar{1}0$ peak. A cut into the 3D reconstruction (a) and 2D cuts (b) taken from this volume. The cross section cut was taken from the line marked (dashed white). This reconstruction gives sensitivity to lattice displacement along $q_{2\bar{1}\bar{1}0}$ (white arrow). The same 2D cross sections converted to strain (ϵ_{11}) (c). Pixels at which the strain derivative wraps over in phase are not shown, as they are non-physical. Red arrows identify the NW facet that was adhered to the Si substrate. All scale bars are 50 nm.

Figure 3(a) shows a section of the nanowire (red box in Figure 2) reconstructed from the $2\bar{1}\bar{1}0$ Bragg peak nanodiffraction patterns. (Details on maBPP phase retrieval of these data are presented in the Algorithm Description section.) Because this Bragg peak is insensitive to stacking faults in this material, the phase of the reconstruction ($\phi_{2\bar{1}\bar{1}0}$) can be

related to the relative displacement of $(2\bar{1}\bar{1}0)$ planes in the direction of the diffraction vector ($u_{2\bar{1}\bar{1}0} = \phi_{2\bar{1}\bar{1}0}/|\mathbf{G_{2\bar{1}\bar{1}0}}|$). 2D cross sections of the displacement fields are shown in 3(b). We note that the reconstruction was performed with the Bragg condition along the white line in Figure 3(b) set as a reference. As a result, this region shows relatively flat phase due to the locally homogeneous structure that evolves axially away from the line due to the twist shown in Figure 2. These same cross sections converted to units of relative compressive/tensile strain along the diffraction vector are shown in 3(c), derived via the spatial derivative $\partial u_{2\bar{1}\bar{1}0}/\partial x_{2\bar{1}\bar{1}0}$,[49] where $x_{2\bar{1}\bar{1}0}$ is defined as the direction normal to the $2\bar{1}\bar{1}0$ planes. Further, analysis of the change of phase along the growth direction reveals that outside a length window of ∼60 nm the lattice orientation varies appreciably (>10 % change) by the twist observed in Figure 2. However, we find that this twist does not strongly influence the strain component $\partial u_{2\bar{1}\bar{1}0}/\partial x_{2\bar{1}\bar{1}0}$, as evidenced by the fact that the strain field across the entire 600 nm window in Figure 3(c) varies by less than $\pm\, 3 \times 10^{-4}$, the 1-σ of the Gaussian distribution of strain values in the volume near the dashed line in Figure 3b. We take this value to be the strain sensitivity limit of this particular measurement, and we note that the striations in strain that fall within this range in Figure 3(c) are artifacts arising from uncertainty in the incident angle of the beam (See Supporting Information (SI) Figure S1). Further, the breadth of strain variations is comparable to strain variations expected from random alloy fluctuations assuming a binomial distribution of group III elements on group III sites (see SI Figure S2). Therefore, we do not expect significant perturbations of the band structure from any long-range strain variations present in these nanowires.

Finally, we note that an isotropic spatial resolution of ∼50 nm in x, y, and z was estimated for this image, commensurate with the 53 nm full-width-at-half-maximum of the amplitude of the probe. In the x and z directions, this was done by fitting the amplitude of the facet edges to an error function. In the y direction, since no sharp features were present in the field of view, the estimate is based on the angular extent of the diffraction patterns, which does not exceed the annulus given by the beam size.

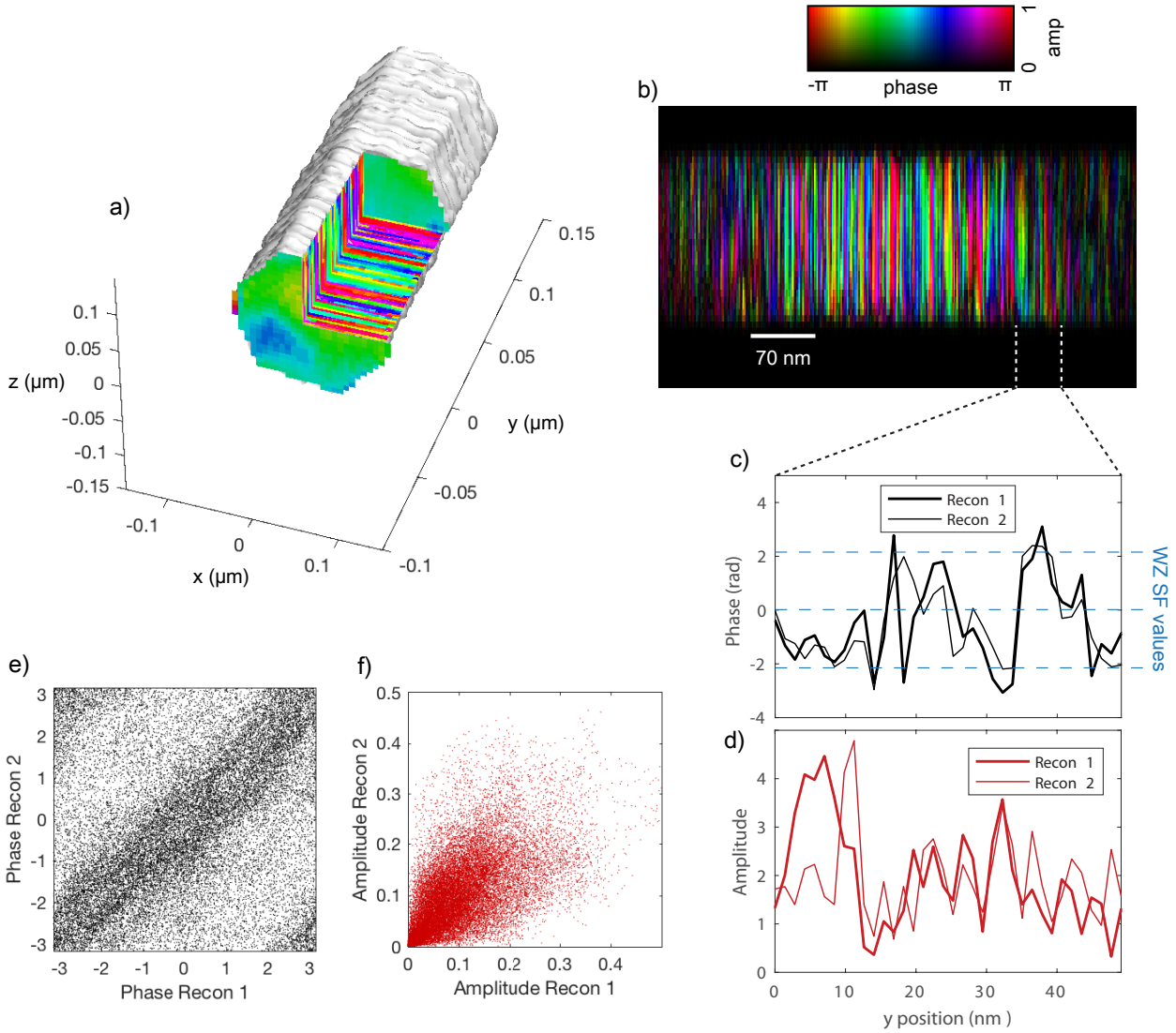

Figure 4: maBPP reconstruction of the $01\bar{1}0$ peak. A cut into the reconstruction volume (a) and a 2D slice (b) reveal rapidly varying phase features. A line cut of phase (c) and intensity (d) from the center of the nanowire compares two independent reconstructions with different starting guesses to test reproducibility. Correlation tables for every point in the two independent reconstructions show strong phase correlation. Note that the wrapping in phase around 2π results in a concentration of points at the top left and bottom right corners which should fall along the correlation axis (e) The two reconstructions show a lesser degree of amplitude correlation (f). The red arrow identifies the NW facet which was adhered to the Si substrate.

In the analysis discussed thus far, nanodiffraction mapping and maBPP have been used to map lattice variations and strain across length scales from a few microns to a few tens of nanometers, but shorter range structure variations in the nanowire can be accessed that have a direct impact on electrical properties. Figure 4(a) shows the 3D reconstruction of the $01\bar{1}0$ Bragg peak that is sensitive to lattice stacking order and strain in the nanowire. The maBPP image contains closely spaced regions of alternating phase and amplitude separated by planar boundaries normal to the growth direction. This morphology is consistent with TEM observations of stacking faults and phase boundaries in closely related nanowire systems.[38] A 2D cut of the phase and amplitude variations along the growth direction is shown in 4(b). The phase color oscillations across stacking fault boundaries (shown as a line cut in Figure 4(c)) correspond roughly with the $[-2\pi/3, 0, 2\pi/3]$ phase shifts expected in the $01\bar{1}0$ Bragg peak structure factor.[43] The $01\bar{1}0$ structure factor is sensitive not only to stacking disorder and crystal phase, but also to changes in lattice orientation and strain. Thus, in this nanowire additional variations in phase beyond those associated with stacking disorder are expected due to the substantial twists in lattice orientation.

The structural information in the $01\bar{1}0$ reconstruction includes multiple components, contains very high spatial frequency information, and thus requires careful consideration. As shown in Figure 2, a typical $01\bar{1}0$ coherent nanodiffraction pattern scatters to very high q_y. Such broad "barcode" interference patterns from stacking faults in nanowires have been observed previously with unfocused coherent beams, and offer the possibility of very high spatial resolution because of scattering to high q_y. In this work, photons were detected to $q_y = 0.48$ Å^{-1}, corresponding to an image pixel size in the y direction of 1.3 nm. (A pixel size of 6.5 nm was used in x and z due to the much more limited extent of scattering observed along q_x and q_z.) However, to date, efforts to invert such diffraction patterns to form an image via standard Bragg coherent diffraction phase retrieval methods have failed due to issues of uniqueness (multiple reconstructions initialized with random numbers yielded different local structures).[20,43] Here, we address this issue in two ways. First, we utilize a

nano-focused beam such that only a few tens of stacking fault boundaries are illuminated per exposure rather than several thousand, as done in previous studies. Second, we use a ptychography approach that more strictly constrains the solution due to the overlap of the beam positions. Both of these factors help to enable reproducible image reconstructions of stacking faults via maBPP (see Figure 4(c-f)).

However, in this particular NW, stacking defects can only be reliably characterized over a limited distance along the growth direction (<50 nm) because of the lattice twist/bend that evolves over the length. Figure 2(c) shows that the Bragg peak maximum (θ_{Br}) changes with position. In maBPP, these variations of θ_{Br} from the prescribed reference angle result in additional phase change in the reconstruction. Figure 3(b) demonstrates how the long-range twist modifies the phase for a given reconstruction of the $2\bar{1}\bar{1}0$ condition. The $01\bar{1}0$ Bragg peak is sensitive to a different component of the same displacement field shown in 3(b). Therefore a phase gradient is present in the resulting reconstruction (Figure 4) in addition to the phase variations associated with WZ stacking faults. Thus, interpreting local phases in terms of stacking faults can only be done over length scales for which phase contributions from other structural phenomena are relatively constant (*e.g* lattice orientation gradients, strain), which is ∼55 nm for the nanowire shown here.

The reconstruction shown in Figure 4(b) demonstrates extraction of nanoscale structure in the presence of these additional contributions. The Bragg condition in this reconstruction was set to correspond to the rocking curve maximum in the region of the nanowire near the white dashed vertical lines. The left half of the image therefore contains rapid pixel-to-pixel phase oscillations due to the superposition of phase contributions from lattice twist, stacking defects, as well as variations due to noise contributions,[50] making direct image interpretation difficult. In envisioning an *in-operando* maBPP study on SF characteristics in such a nanowire, more advanced analytical tools are needed that can decouple the components of lattice strain from stacking defects using multiple maBPP images of the same volume, enabling larger fields of view to be interrogated.

Nevertheless, within a 50 nm field of view along the wire axis, as shown, these complicating factors are minimized, and several stacking fault boundaries can be reproducibly imaged. To demonstrate this, phase and amplitude from two different randomly initiated reconstructions (Recon 1,2) are compared for the region denoted in Figure 4(b). Line-outs from this region (4(c,d)) reproduce well, and a strong correlation is seen for all voxels in the volume bounded by planes parallel to the dotted lines (4(e,f)). Within this field of view we can identify ∼10 WZ stacking fault boundaries that result in $[-2\pi/3, 0, 2\pi/3]$ phase values. The amplitude in this reconstruction is sensitive to ZB phase, but because the ZB inclusions are expected to persist over very small distances (< 1 nm), they will be under-resolved in this image. Given the observation of realistic features expected for these nanowires[38] on the scale as small as 2 pixels, we conservatively estimate an upper bound resolution along the wire axis of 2.6 nm (2× pixel size). (SI Figure S3 shows reconstructions from simulations of a lower stacking fault density nanowire in which this spatial resolution estimate is more clearly demonstrated.) We note that many if not most III-As nanowires can be grown with a much lower density of stacking defects than the nanowire imaged here, suggesting that the maBPP methodology can be usefully applied to correlate defect density and electronic properties in many nanowire systems of interest. Finally, as in the $2\bar{1}\bar{1}0$ reconstruction, the average resolution along the x and z directions was found to be ∼50 nm consistent with the limited angular extent of scattering along q_x and q_z. As is in any ptychography experiments, improvements in resolution can be obtained with improved signal-to-noise ratios of the diffraction signal, especially in regions that extend beyond the beam-limited annulus in reciprocal space.

In conclusion, we demonstrated the ability to image a single InGaAs nanowire on many length scales with sensitivity to multiple nanoscale lattice features. In analyzing and reconstructing diffraction patterns from the $2\bar{1}\bar{1}0$ Bragg peak, we found that the lattice orientation varied along the length of the wire at micron length scales and that the strain field along the wire cross-section was largely unaffected by this long range lattice rotation. Using diffraction

patterns measured from the same wire at the $01\bar{1}0$ Bragg peak, we could reproducibly reconstruct images of stacking defects. This reconstruction evidenced sharp planar boundaries between different crystal phases of WZ structure, as expected. In both cases, phase retrieval was made possible by a multi-angle Bragg projection ptychography approach that accommodates coherent nanodiffraction patterns measured at arbitrary overlapping positions at multiple angles about a Bragg peak, eliminating the need for scan registration at different angles which is impractical with nanobeams. In combination with coarse scanning nanodiffraction measurements, maBPP allowed for structural investigation of a nanowire over three decades of length spanning from several microns to tens of angstroms. By enabling such a capability, maBPP can contribute significantly to our understanding of nanowires and other nanostructures by correlating structure and properties. This capability will be especially complementary to electron microscopy of nanowires on transparent supports and post-operando atom probe tomography of nanowires embedded in devices, and improvements in maBPP spatial resolution and strain sensitivity can be achieved with further development of the method, for example, by implementing simultaneous probe and sample reconstruction.

Algorithm Description: maBPP is predicated on a description of coherent scattering from a nanoscale crystal that equates the far-field diffracted intensity pattern measured with an area detector to a general probe position and measurement angle relative to the Bragg peak. These two degrees of freedom, position and angle, are illustrated in Figure 1(b,c). A monochromatic beam illuminating a crystal will satisfy a Bragg condition when the scattering vector $\mathbf{q} = \mathbf{k_f} - \mathbf{k_i}$ coincides with a Bravais lattice point $\mathbf{G_{HKL}}$ of the illuminated crystal. (Here, $|\mathbf{k}| = 2\pi/\lambda$ where λ is the x-ray wavelength.) Small angular deviations from this condition can be expressed in terms of $\mathbf{Q} = \mathbf{q} - \mathbf{G}$. As described in other work, this vector $\mathbf{Q}$ encodes changes in a coherent diffraction pattern due to angular variations along a Bragg rocking curve.[51,52] A focused-beam nanodiffraction experiment also allows the incident beam to scan a given region of interest in a crystal by scanning the probe position relative to the sample (in this case, using sample stage motors x_{mot}, y_{mot}). Thus, a general Bragg

ptychography data set for a given field of view comprises of $j = 1 \cdots J$ two-dimensional coherent diffraction intensity patterns I_j measured as a function of different probe positions ($\mathbf{r}_j$) at various angles relative to the Bragg peak (θ_j).

Each of these intensity patterns is the squared modulus of the diffracted wave field at the detector, $I_j = |\psi_j|^2$. The quantity ψ_j can be generally expressed in a maBPP experiment as:

$$\psi_j = \mathcal{F}\mathcal{R}\mathcal{Q}_{\theta_j} P_{\mathbf{r}_j} \rho. \tag{1}$$

Here, $P_{\mathbf{r}_j}$ is the 3D wave field of the focused x-ray probe positioned to illuminate the crystal ρ according to the translation of the sample stage motors (x_{mot}, y_{mot}). The term $\mathcal{Q}_{\theta_j} = \exp[i\,\mathbf{r} \cdot \mathbf{Q}_{\theta_j}]$ (where $i = \sqrt{-1}$) is a 3D real-space complex-valued phase term that encodes spatial frequencies corresponding to angular deviations from θ_{Br}, where θ_{Br} is the angle that satisfies the Bragg condition of the crystal. $\mathcal{R}$ is a 3D$\rightarrow$2D projection along the $\mathbf{k_f}$ direction, and $\mathcal{F}$ is a 2D Fourier transformation. This construction of ψ_j leads to a general description of a Bragg ptychography data set in which the probe position and angle are arbitrary and need not be otherwise related so long as the typical degree of probe overlap ($\sim$ 50%) is enforced. In a manner similar to References 24 and 51, Equation 1 can be used to derive a gradient that minimizes the sum squared error $\epsilon^2 = \sum_j \parallel |\psi_j| - \sqrt{I_j} \parallel^2$ and that can be incorporated into phase retrieval algorithms such as the Ptychgraphic Iterative Engine (PIE) to reconstruct a 3D image, as was done in this work.

For the maBPP data sets measured at the two Bragg peaks featured in this work, diffraction maps from only strongly scattering angles (indicated in red in Figure 2(a) and (b)) were used for image reconstruction. 25 iterations of maBPP with PIE were performed, and a hexagonal-shaped 3D support was used corresponding to the facet orientation of the SEM image in Figure 1(a). The diameter of the support for the $2\bar{1}\bar{1}0$ and $01\bar{1}0$ reconstructions was, respectively, 180% and 130% of the nominal wire diameter.

Associated Content

Supporting Information Available: Document describing 1) the effect of angular uncertainty on a maBPP experiment, 2) simulation of strain induced by composition variations due to random alloying, and 3) a maBPP reconstruction of a simulated nanowire with random stacking faults as compared to the original structure.

Acknowledgments

Development of maBPP phase retrieval and synchrotron measurements were supported by the U.S. Department of Energy (DOE), Office of Basic Energy Sciences (BES), Materials Science and Engineering Division. maBPP modeling, phase retrieval of experimental InGaAs data, and SEM characterization was supported by NSF DMR-1611341, acknowledged by L.J.L. and M.O.H. M.O.H. also acknowledges tuition and salary support of the NSF GRFP. V.C. and M.A. acknowledge funding from the European Research Council (ERC) under the European Union's Horizon H2020 research and innovation programme grant agreement No 724881. M.V.H. acknowledges support from the Center for Nanoscale Materials, a U.S. Department of Energy Office of Science User Facility supported by the U.S. Department of Energy, Office of Science, under Contract No. DE-AC02-06CH11357. G.K. aknowledges financial support by the German Research Foundation (DFG), the Nanosystems Initiative Munich (NIM), and the Technical University of Munich, Institute for Advanced Study. This work made use of the EPIC facility of Northwestern Universitys NUANCE Center, which has received support from the Soft and Hybrid Nanotechnology Experimental (SHyNE) Resource (NSF ECCS-1542205); the MRSEC program (NSF DMR-1121262) at the Materials Research Center; the International Institute for Nanotechnology (IIN); the Keck Foundation; and the State of Illinois, through the IIN. This research used the Hard X-ray Nanoprobe (HXN) Beamline at 3-ID of the National Synchrotron Light Source II, a U.S. Department of Energy (DOE) Office of Science User Facility operated for the DOE Office of Science by Brookhaven

National Laboratory under Contract No. DE-SC0012704.

References

(1) Koblmüller, G.; Abstreiter, G. *Phys. Status Solidi RRL* **2014**, *8*, 11–30. DOI: 10.1002/pssr.201308207.

(2) Kim, H.; Lee, W.-J.; Farrell, A. C.; Morales, J. S.; Senanayake, P. N.; Prikhodko, S. V.; Ochalski, T.; Huffaker, D. L. *Nano Lett.* **2017**, *17*, 3465–3470. DOI: 10.1021/acs.nanolett.7b00384.

(3) Shen, L.; Pun, E. Y.; Ho, J. C. *Mater. Chem. Front.* **2017**, *1*, 630–645. DOI: 10.1039/C6QM00279J.

(4) Li, N.; Liu, K.; Sorger, V. J.; Sadana, D. K. *Sci. Rep.* **2015**, *5*, 14067. DOI: 10.1038/srep14067.

(5) Mårtensson, T.; Svensson, C. P. T.; Wacaser, B. A.; Larsson, M. W.; Seifert, W.; Deppert, K.; Gustafsson, A.; Wallenberg, L. R.; Samuelson, L. *Nano Lett.* **2004**, *4*, 1987–1990. DOI: 10.1021/nl0487267.

(6) Koblmüller, G.; Mayer, B.; Stettner, T.; Abstreiter, G.; Finley, J. J. *Semicond. Sci. Tech.* **2017**, *32*, 053001. DOI: 10.1088/1361–6641/aa5e45.

(7) LaPierre, R.; Robson, M.; Azizur-Rahman, K.; Kuyanov, P. *J. Phys. D Appl. Phys.* **2017**, *50*, 123001. DOI: 10.1088/1361–6463/aa5ab3.

(8) Spirkoska, D.; Arbiol, J.; Gustafsson, A.; Conesa-Boj, S.; Glas, F.; Zardo, I.; Heigoldt, M.; Gass, M.; Bleloch, A. L.; Estrade, S. *Phys. Rev. B* **2009**, *80*, 245325. DOI: 10.1103/PhysRevB.80.245325.

(9) Verheijen, M. A.; Algra, R. E.; Borgström, M. T.; Immink, G.; Sourty, E.; van Enckevort, W. J.; Vlieg, E.; Bakkers, E. P. *Nano Lett.* **2007**, *7*, 3051–3055. DOI: 10.1021/nl071541q.

(10) Rudolph, D.; Funk, D., Stefan; Markus,; Morkötterr, S.; Hertenberger, S.; Schweickert, L.; Becker, J.; Matich, S.; Bichler, M.; Spirkoska, D. *Nano Lett.* **2013**, *13*, 1522–1527. DOI: 10.1021/nl3046816.

(11) Jeon, N.; Loitsch, B.; Morkötter, S.; Abstreiter, G.; Finley, J.; Krenner, H. J.; Koblmüller, G.; Lauhon, L. J. *ACS Nano* **2015**, *9*, 8335–8343. DOI: 10.1021/acsnano.5b04070.

(12) Schroer, M. D.; Petta, J. R. *Nano Lett.* **2010**, *10*, 1618–1622. DOI: 10.1021/nl904053j.

(13) Irber, D. M.; Seidl, J.; Carrad, D. J.; Becker, J.; Jeon, N.; Loitsch, B.; Winnerl, J.; Matich, S.; Dblinger, M.; Tang, Y.; Morktter, S.; Abstreiter, G.; Finley, J. J.; Grayson, M.; Lauhon, L. J.; Koblmller, G. *Nano Lett.* **2017**, *17*, 4886–4893. DOI: 10.1021/acs.nanolett.7b01732.

(14) Jahn, U.; Lähnemann, J.; Pfüller, C.; Brandt, O.; Breuer, S.; Jenichen, B.; Ramsteiner, M.; Geelhaar, L.; Riechert, H. *Phys. Rev. B* **2012**, *85*, 045323. DOI: 10.1103/PhysRevB.85.045323.

(15) Loitsch, B.; Winnerl, J.; Grimaldi, G.; Wierzbowski, J.; Rudolph, D.; Morkotter, S.; Doblinger, M.; Abstreiter, G.; Koblmuller, G.; Finley, J. J. *Nano letters* **2015**, *15*, 7544–7551. DOI:10. 1021/acs.nanolett.5b03273.

(16) Dzhigaev, D.; Stankevic, T.; Bi, Z.; Lazarev, S.; Rose, M.; Shabalin, A.; Reinhardt, J.; Mikkelsen, A.; Samuelson, L.; Falkenberg, G. *ACS Nano* **2017**, *11*, 6605–6611. DOI: 10.1021/acsnano.6b08122.

(17) Davtyan, A.; Krause, T.; Kriegner, D.; Al-Hassan, A.; Bahrami, D.; Mostafavi Kashani, S.; Lewis, R. B.; Küpers, H.; Tahraoui, A.; Geelhaar, L. *J. Appl. Crystallogr.* **2017**, *50*, 673–680. DOI: 10.1107/S1600576717004149.

(18) Diaz, A.; Mocuta, C.; Stangl, J.; Mandl, B.; David, C.; Vila-Comamala, J.; Chamard, V.; Metzger, T.; Bauer, G. *Phys. Rev. B* **2009**, *79*, 125324. DOI: 10.1103/PhysRevB.79.125324.

(19) Labat, S.; Richard, M.-I.; Dupraz, M.; Gailhanou, M.; Beutier, G.; Verdier, M.; Mastropietro, F.; Cornelius, T. W.; Schülli, T. U.; Eymery, J.; Thomas, O. *ACS Nano* **2015**, *9*, 9210–9216. DOI: 10.1021/acsnano.5b03857.

(20) Davtyan, A.; Biermanns, A.; Loffeld, O.; Pietsch, U. *New J. Phys.* **2016**, *18*, 063021. DOI: 10.1088/1367–2630/18/6/063021.

(21) Davtyan, A.; Lehmann, S.; Kriegner, D.; Zamani, R. R.; Dick, K. A.; Bahrami, D.; Al-Hassan, A.; Leake, S. J.; Pietsch, U.; Holỳ, V. *J. Synchrotron Radiat.* **2017**, *24*, 981–990. DOI: 10.1107/S1600577517009584.

(22) Treu, J.; Speckbacher, M.; Saller, K.; Morkötter, S.; Döblinger, M.; Xu, X.; Riedl, H.; Abstreiter, G.; Finley, J.; Koblmüller, G. *Appl. Phys. Lett.* **2016**, *108*, 053110. DOI: 10.1063/1.4941407.

(23) Treu, J.; Stettner, T.; Watzinger, M.; Morkötter, S.; Doeblinger, M.; Matich, S.; Saller, K.; Bichler, M.; Abstreiter, G.; Finley, J. J.; Stangl, J.; Koblmüller, G. *Nano Lett.* **2015**, *15*, 3533–3540. DOI: 10.1021/acs.nanolett.5b00979.

(24) Hruszkewycz, S. O.; Allain, M.; Holt, M. V.; Murray, C. E.; Holt, J. R.; Fuoss, P. H.; Chamard, V. *Nat. Mater.* **2016**, *16*, 244–251. DOI: 10.1038/nmat4798.

(25) Godard, P.; Carbone, G.; Allain, M.; Mastropietro, F.; Chen, G.; Capello, L.;

Diaz, A.; Metzger, T. H.; Stangl, J.; Chamard, V. *Nat. Commun.* **2011**, *2*, 568. DOI: 10.1038/ncomms1569.

(26) Rodenburg, J. M.; Hurst, A. C.; Cullis, A. G.; Dobson, B. R.; Pfeiffer, F.; Bunk, O.; David, C.; Jefimovs, K.; Johnson, I. *Phys. Rev. Lett.* **2007**, *98*, 034801. DOI: 10.1103/PhysRevLett.98.034801.

(27) Thibault, P.; Dierolf, M.; Menzel, A.; Bunk, O.; David, C.; Pfeiffer, F. *Science* **2008**, *321*, 379–382. DOI: 10.1126/science.1158573.

(28) Godard, P.; Allain, M.; Chamard, V.; Rodenburg, J. *Opt. Express* **2012**, *20*, 25914–25934. DOI: 10.1126/science.1158573.

(29) Holt, M. V.; Hruszkewycz, S. O.; Murray, C. E.; Holt, J. R.; Paskiewicz, D. M.; Fuoss, P. H. *Phys. Rev. Lett.* **2014**, *112*, 165502. DOI: 10.1103/PhysRevLett.112.165502.

(30) Ulvestad, A.; Clark, J. N.; Harder, R.; Robinson, I. K.; Shpyrko, O. G. *Nano Lett.* **2015**, *15*, 4066–4070, DOI: 10.1021/acs.nanolett.5b01104.

(31) Munkholm, A.; Thompson, C.; Foster, C. M.; Eastman, J. A.; Auciello, O.; Stephenson, G. B.; Fini, P.; DenBaars, S. P.; Speck, J. S. *Appl. Phys. Lett.* **1998**, *72*, 2972–4. DOI: 10.1063/1.121511.

(32) Takahashi, Y.; Suzuki, A.; Furutaku, S.; Yamauchi, K.; Kohmura, Y.; Ishikawa, T. *Phys. Rev. B* **2013**, *87*, 121201. DOI: 10.1103/PhysRevB.87.121201.

(33) Hruszkewycz, S. O.; Highland, M. J.; Holt, M. V.; Kim, D.; Folkman, C. M.; Thompson, C.; Tripathi, A.; Stephenson, G. B.; Hong, S.; Fuoss, P. H. *Phys. Rev. Lett.* **2013**, *110*, 177601. DOI: 10.1103/PhysRevLett.110.177601.

(34) Pateras, A. I.; Allain, M.; Godard, P.; Largeau, L.; Patriarche, G.; Talneau, A.; Pantzas, K.; Burghammer, M.; Minkevich, A. A.; Chamard, V. *Phys. Rev. B* **2015**, *92*, 205305–11. DOI: 10.1103/PhysRevB.92.205305.

(35) Pelz, P. M.; Guizar-Sicairos, M.; Thibault, P.; Johnson, I.; Holler, M.; Menzel, A. *Appl. Phys. Lett.* **2014**, *105*, 251101. DOI: 10.1063/1.4904943.

(36) Clark, J. N.; Huang, X.; Harder, R. J.; Robinson, I. K. *Opt. Lett.* **2014**, *39*, 6066–6069. DOI: 10.1364/OL.39.006066P.

(37) Hruszkewycz, S. O.; Holt, M. V.; Murray, C. E.; Bruley, J.; Holt, J.; Tripathi, A.; Shpyrko, O. G.; Mcnulty, I.; Highland, M. J.; Fuoss, P. H. *Nano Lett.* **2012**, *12*, 5148–5154. DOI: 10.1021/nl303201w.

(38) Morkötter, S.; Funk, S.; Liang, M.; Doeblinger, M.; Hertenberger, S.; Treu, J.; Rudolph, D.; Yadav, A.; Becker, J.; Bichler, M.; Scarpa, G.; Lugli, P.; Zardo, I.; Finley, J. J.; Abstreiter, G.; Koblmüller, G. *Phys. Rev. B* **2013**, *87*, 205303. DOI: 10.1103/PhysRevB.87.205303.

(39) Saxena, D.; Mokkapati, S.; Parkinson, P.; Jiang, N.; Gao, Q.; Tan, H. H.; Jagadish, C. *Nat. Photonics* **2013**, *7*, 963–968 DOI: 10.1038/nphoton.2013.303.

(40) Yan, H.; Nazaretski, E.; Lauer, K.; Huang, X.; Wagner, U.; Rau, C.; Yusuf, M.; Robinson, I.; Kalbfleisch, S.; Li, L. *Sci. Rep.* **2016**, *6*, 20112. DOI: 10.1038/srep20112.

(41) Nazaretski, E.; Lauer, K.; Yan, H.; Bouet, N.; Zhou, J.; Conley, R.; Huang, X.; Xu, W.; Lu, M.; Gofron, K.; Kalbfleisch, S.; Wagner, U.; Rau, C.; Chu, Y. S. *J. Synchrotron Radiat.* **2015**, *22*, 1–6. DOI: 10.1107/S1600577514025715.

(42) Nazaretski, E.; Yan, H.; Lauer, K.; Bouet, N.; Huang, X.; Xu, W.; Zhou, J.; Shu, D.; Hwu, Y.; Chu, Y. S. *J. Synchrotron Radiat.* **2017**, *24*, 1113–1119. DOI:10.1107/S1600577517011183.

(43) Favre-Nicolin, V.; Mastropietro, F.; Eymery, J.; Camacho, D.; Niquet, Y. M.; Borg, B. M.; Messing, M. E.; Wernersson, L.-E.; Algra, R. E.; Bakkers, E. P.

A. M.; Metzger, T. H.; Harder, R.; Robinson, I. K. *New J. Phys.* **2010**, *12*, 035013. DOI:10.1088/1367–2630/12/3/035013.

(44) Hruszkewycz, S. O.; Holt, M. V.; Allain, M.; Chamard, V.; Polvino, S. M.; Murray, C. E.; Fuoss, P. H. *Opt. Lett.* **2015**, *40*, 3241. DOI: 10.1364/OL.40.003241.

(45) Stankevič, T.; Hilner, E.; Seiboth, F.; Ciechonski, R.; Vescovi, G.; Kryliouk, O.; Johansson, U.; Samuelson, L.; Wellenreuther, G.; Falkenberg, G. *ACS Nano* **2015**, *9*, 6978–6984. DOI: 10.1021/acsnano.5b01291.

(46) Dzhigaev, D.; Shabalin, A.; Stankevič, T.; Lorenz, U.; Kurta, R.; Seiboth, F.; Wallentin, J.; Singer, A.; Lazarev, S.; Yefanov, O.; , M. N. S. L. S. G. F. C. G. S. A. M. R. F., M Borgström; Vartanyants, I. A. *J.Opt.* **2016**, *18*, 064007. DOI: 10.1088/2040–8978/18/6/064007.

(47) Wallentin, J.; Jacobsson, D.; Osterhoff, M.; Borgström, M. T.; Salditt, T. *Nano Lett.* **2017**, *17*, 4143–4150. DOI: 10.1021/acs.nanolett.7b00918.

(48) Wallander, H.; Wallentin, J. *J. Synchrotron Radiat.* **2017**, *24*, 925–933. DOI: 10.1107/S1600577517008712.

(49) Ulvestad, A.; Singer, A.; Clark, J. N.; Cho, H. M.; Kim, J. W.; Harder, R.; Maser, J.; Meng, Y. S.; Shpyrko, O. G. *Science* **2015**, *348*, 1344–1347. DOI: 10.1126/science.aaa1313.

(50) Mastropietro, F.; Godard, P.; Burghammer, M.; Chevallard, C.; Daillant, J.; Duboisset, J.; Allain, M.; Guenoun, P.; Nouet, J.; Chamard, V. *Nat. Mater.* **2017**, *9*, 946–952. DOI: 10.1038/nmat4937.

(51) Cha, W.; Ulvestad, A.; Allain, M.; Chamard, V.; Harder, R.; Leake, S. J.; Maser, J.; Fuoss, P. H.; Hruszkewycz, S. O. *Phys. Rev. Lett.* **2016**, *117*, 225501–5. DOI: 10.1103/PhysRevLett.117.225501.

(52) Dzhigaev, D.; Stankevič, T.; Besedin, I.; Lazarev, S.; Shabalin, A.; Strikhanov, M. N.; Feidenhans, R.; Vartanyants, I. A. *Proc. SPIE* **2015**, *9592*, 95920S–95920S. DOI: 10.1117/12.2190416.

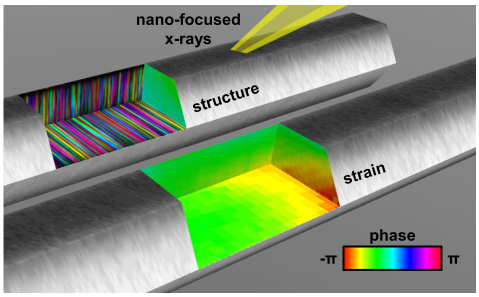

TOC Figure